Vitamin D Receptor Activation and Photodynamic Priming Enables Durable Low-dose Chemotherapy

Sriram Anbil[1,2], Michael Pigula[2], Huang-Chiao Huang[2], Srivalleesha Mallidi[2], Mans Broekgaarden[2], Yan Baglo[2], Pushpamali De Silva[2], Diane M. Simeone[3], Mari Mino-Kenudson[4], Edward V. Maytin[5], Imran Rizvi[2], and Tayyaba Hasan[2,6]

ABSTRACT

Patients with cancer often confront the decision of whether to continue high-dose chemotherapy at the expense of cumulative toxicities. Reducing the dose of chemotherapy regimens while preserving efficacy is sorely needed to preserve the performance status of these vulnerable patients, yet has not been prioritized. Here, we introduce a dual pronged approach to modulate the microenvironment of desmoplastic pancreatic tumors and enable significant dose deescalation of the FDA-approved chemotherapeutic nanoliposomal irinotecan (nal-IRI) without compromising tumor control. We demonstrate that light-based photodynamic priming (PDP) coupled with vitamin D3 receptor (VDR) activation within fibroblasts increases intratumoral nal-IRI accumulation and suppresses protumorigenic CXCL12/CXCR7 crosstalk. Combined photodynamic and biochemical modulation of the tumor microenvironment enables a 75% dose reduction of nal-IRI while maintaining treatment efficacy, resulting in improved tolerability. Modifying the disease landscape to increase the susceptibility of cancer, via preferentially modulating fibroblasts, represents a promising and relatively underexplored strategy to enable dose deescalation. The approach presented here, using a combination of three clinically available therapies with nonoverlapping toxicities, can be rapidly translated with minimal modification to treatment workflow, and challenges the notion that significant improvements in chemotherapy efficacy can only be achieved at the expense of increased toxicity.

Introduction

Patients with advanced pancreatic ductal adenocarcinoma (PDAC) present with significant comorbidities and poor performance status. Improved survival outcomes for these patients are contingent upon their ability to withstand prolonged toxic treatment regimens (1). Deteriorating performance status coupled with treatment induced toxicities prevents many of these patients from initiating or completing preferred regimens. Even the most recent clinical trials for this disease, including those utilizing stromal depletion, continue to yield unfavorable outcomes at the expense of significant toxicity (2), highlighting the dire need to translate strategies that improve the tolerability of anticancer regimens while also preserving their efficacy (1).

We introduce a multimodal approach comprised of photodynamic priming (PDP) and vitamin D receptor (VDR) activation to modulate the microenvironment of PDAC and increase its susceptibility to cytotoxic therapies. We demonstrate that subcytotoxic PDP, a photochemistry-based therapeutic modality, combined with the vitamin D analogue Calcipotriol (CAL) suppresses protumorigenic intratumoral paracrine signaling interactions and permeabilizes the tumor-associated microvasculature and parenchyma to significantly improve the anticancer effects of nanoliposomal irinotecan (nal-IRI). This priming regimen, which consists of two clinically approved agents with distinct mechanisms of action and nonoverlapping toxicities, enables a 75% dose deescalation of nal-IRI while maintaining durable anticancer efficacy and tolerability.

Shortcomings in treatment response are increasingly attributed to tumor heterogeneity, poor drug delivery, and disease-sustaining intratumoral paracrine interactions that involve the microenvironment (3). For advanced PDAC, only modest improvements in survival have been achieved despite the administration of consecutive multimodal chemotherapies at the maximum tolerated dose, in part because the tumor microenvironment is not addressed (4, 5). Shifting focus away from consecutive high-dose chemotherapeutics towards less toxic strategies that modify the disease landscape may enable chemotherapy dose reduction without negatively impacting efficacy. Photodynamic therapy (PDT) is a photochemistry-based modality in which a photosensitizer is activated by light of a specific wavelength to produce local reactive molecular species (RMS), and is currently being evaluated clinically as an adjuvant to surgery and chemotherapy in patients with advanced PDAC (refs. 6, 7; NCT03033225). PDP is a companion effect of PDT that occurs when the RMS produced by photodynamic activation do not surpass the cytotoxic threshold. Counterintuitively,

[1]Long School of Medicine, UT Health San Antonio, San Antonio, Texas. [2]Wellman Center for Photomedicine, Massachusetts General Hospital and Harvard Medical School, Boston, Massachusetts. [3]Department of Surgery, Langone School of Medicine, New York University, New York, New York. [4]Department of Pathology, Massachusetts General Hospital and Harvard Medical School, Boston, Massachusetts. [5]Department of Dermatology and Department of Biomedical Engineering, Cleveland Clinic, Cleveland, Ohio. [6]Division of Health Sciences and Technology, Harvard University and Massachusetts Institute of Technology, Cambridge, MA.

Note: Supplementary data for this article are available at Molecular Cancer Therapeutics Online (http://mct.aacrjournals.org/).

S. Anbil and M. Pigula contributed equally to this article.

Current address for S. Anbil: David Geffen School of Medicine, University of California Los Angeles, Los Angeles, California; current address for H.-C. Huang and Y. Baglo, Fischell Department of Bioengineering, University of Maryland, College Park, Maryland; current address for S. Mallidi, Department of Biomedical Engineering, Tufts University, Medford, Massachusetts; and current address for I. Rizvi, Joint Department of Biomedical Engineering, The University of North Carolina at Chapel Hill and North Carolina State University, Chapel Hill, North Carolina.

Corresponding Author: Tayyaba Hasan, Massachusetts General Hospital, 40 Blossom Street, BAR 314A, Boston, MA 02114. Phone: 617-726-6996; Fax: 617-724-1345; E-mail: thasan@mgh.harvard.edu

Mol Cancer Ther 2020;19:1308–19

doi: 10.1158/1535-7163.MCT-19-0791

subthreshold RMS can actually be advantageous and have been shown to modulate cancer cells and the surrounding stroma to sensitize tumors to chemotherapy (8, 9), improve chemotherapeutic delivery by inducing intravascular and intratumoral permeabilization (10, 11), yield significant anticancer immune stimulatory effects (12), and avoid dangerous evolutionary selection pressures imparted by high-dose chemotherapy regimens (10, 13). PDP is therefore an attractive strategy to enhance the efficacy of conventional chemotherapeutic regimens (13, 14).

Targeting the interactions between tumor cells and their microenvironment may enhance patient outcomes. For PDAC, the tumor-associated microenvironment is known to comprise a majority of the tumor, and these stromal components are a major driver of disease progression (15). Abundant within the PDAC desmoplasia are cancer-associated fibroblasts (CAF), which have been confirmed in numerous reports to contribute to poor treatment outcomes by promoting fibrosis, altering tumor metabolism, increasing metastasis, and suppressing immunogenicity (4, 16). CAL has been shown to effectively modulate the PDAC associated microenvironment by inducing a variety of epigenetic and transcriptomic changes in cancer-associated pancreatic stellate cells (CAPSC), a CAF precursor, consistent with their "reprogramming" to a noncancer associated, or quiescent, state (17, 18). On the basis of this strategy, multiple clinical trials utilizing vitamin D analogues in combination with conventional chemo- or immunotherapies are ongoing for patients with resectable or metastatic PDAC (NCT03331562, NCT03300921, NCT03520790, NCT03519308).

Vitamin D (17) and PDP (19, 20) have been shown to modulate a number of chemokines in various disease contexts including the C-X-C and C-C pathways, several of which have been implicated in PDAC progression (21). In one example, secretion of the C-X-C motif chemokine 12 (CXCL12, also known as stromal derived factor 1, or SDF-1) by stromal cells, namely stellate cells and fibroblasts, triggers a variety of aggressive phenotypes in PDAC cells, including epithelial-to-mesenchymal transition, chemoresistance, proliferation, angiogenesis, and suppression of antitumor T-cell activity, following its interaction with C-X-C motif receptors 4 and 7 [CXCR4 and CXCR7 (or atypical chemokine receptor 3 - ACKR3); refs. 22, 23]. We demonstrate that combined PDP and CAL treatment reduces CXCL12 secretion by CAFs, suppressing this pro-tumorigenic signaling axis.

We present a quickly translatable approach that integrates both efficacy and tolerability for patients by combining PDP with biochemical stromal reprogramming as a priming strategy for chemotherapy. Simultaneous modulation of the tumor-associated vasculature and stroma, in part, via suppression of the CXCL12/CXCR4/CXCR7 signaling, is demonstrated to markedly enhance the efficacy and tolerability of a widely used chemotherapy, and enable significant dose deescalation while maintaining efficacy and tolerability.

Materials and Methods

Cell culture

All cells were cultured in L-Glutamine containing DMEM (Corning 10-013-CV) supplemented with 10% FBS and 100 U/mL penicillin, 100 μg/mL streptomycin (Gibco, Thermo Fisher Scientific), and maintained in a humidified CO_2 atmosphere at 37°C. MIA-PaCa-2, AsPC-1, and MRC-5 were purchased from the ATCC. SCCAFs were obtained from the Department of Dermatology, Massachusetts General Hospital (MGH, Boston, MA), following isolation from discarded squamous cell carcinoma tissue as approved by the IRB. PCAFs were isolated from tumors of patients who underwent surgical resection at the University of Michigan Hospital (Ann Arbor, MI; ref. 24). All cells were confirmed negative for *Mycoplasma* (Lonza MycoAlert) prior to initial use and every 3 months thereafter.

Orthotopic mouse model, treatments, and toxicology studies

All treatments, procedures, and handling of animals were in accordance with the protocol approved by MGH IACUC. MIA-PaCa-2 cells and/or PCAFs were orthotopically implanted into the pancreas of 4–6 week old male Swiss nude mice (20–25 g). Animals were anesthetized with ketamine/xylazine, and a small left abdominal flank incision was made to exteriorize the pancreas. A 50 μL media + Matrigel (BD Biosciences) suspension of 1×10^6 MIA-PaCa-2, or 5×10^5 MIA-PaCa-2 and 5×10^5 PCAFs (co-implantation model) was injected into the pancreas. Calcipotriol (100 μg/kg, intraperitoneal, Tocris) was administered daily on days 5–8 and 10–13 postimplantation in 1 mL sterile saline. Injections of Visudyne (liposomal verteporfin, 0.25 mg/kg, i.v.) and/or nal-IRI (5, 10 or 20 mg/kg, i.v., Ipsen) were performed on day 9 in 200 μL sterile PBS, simultaneously when applicable. One hour after the injection of Visudyne, PDP was performed to the exteriorized pancreas using a 690 nm diode laser (High Power Devices) delivered at an irradiance of 100 mW/cm^2 to achieve a fluence of 75 J/cm^2. A one-hour drug light interval was selected because there is a balanced distribution of photosensitizer in the tumor-associated microvasculature and parenchyma at this time point. Mice were randomized into treatment groups, and tumor growth was longitudinally monitored using ultrasound imaging as described previously (25). Mouse blood was collected 48 hours post PDP and/or nal-IRI treatment, and analyzed by staff at the MGH CCM Clinical Pathology Laboratory using a DriChem analyzer.

Immunofluorescence imaging of CXCL12, CXCR7, CXCR4, and vitamin D receptor

Anti-CXCL12 (R&D systems, Alexa Fluor 488 conjugated, clone 79018), CXCR7 (R&D systems, PE-conjugated, clone 358426) and CXCR4 antibodies (R&D systems, PE-conjugated, clone 12G5) were used for immunofluorescence experiments. Orthotopic pancreatic tumors were harvested immediately following treatment (15 days after implantation) or 76 days after treatment (90 days after tumor implantation), and prepared as described previously (10). Confocal fluorescence imaging was performed using an Olympus FluoView 1000 confocal microscope with a 20 × 0.75NA objective. Excitation of DAPI, Alexa Fluor 488, APC, and Alexa Fluor 647 fluorophores was carried out using 405-, 405-, and 635-nm lasers, respectively, with appropriate filters. Six to 10 images, evenly distributed across the tumor cross-section, were collected from at least two tumor samples for each condition. Fluorescence was quantified as described previously (10). For analysis of VDR activation, cells were cultured in a glass bottom 24-well plate for 72 hours and treated with 1 μmol/L calcipotriol. Twenty-four hours later, cells were fixed with 1:1 acetone: methanol for 5 minutes, washed with PBS, and incubated with blocking solution (DAKO protein block) for 30 minutes followed by anti-VDR antibody (1:1,000, Abcam, ab3508) overnight at 4°C. Secondary goat anti-rabbit IgG (Abcam, 1:500, Alexa Fluor 488 conjugated, ab150077) was applied, cells were washed with PBS, mounted (Invitrogen SlowFade Gold with 4′,6-diamidino-2-phenylindole, DAPI) with a round glass coverslip, and imaged with an Olympus FluoView 1000 confocal microscope with a 40× objective. Five images, evenly distributed across each well were taken per well, with 15 images taken per condition. The dynamic range for each laser line described was established with an unstained background control.

In vitro CXCL12 secretion and conditioned medium assays

CXCL12 secretion from PDAC and fibroblast lines was evaluated by ELISA (Abcam, ab100637). Cells were cultured for 96 hours in serum free DMEM, at which point wells were 50%–80% confluent. Supernatant was collected and processed per kit specifications and standard curves were generated using recombinant CXCL12 provided by the manufacturer. Treatment was performed 24 hours after plating. For PDP, cells were incubated with 0.25 μmol/L BPD for 90 minutes in culture medium. Medium was then replaced and cells were irradiated with 690 nm light (Intense Ltd.) at an irradiance of 150 mW/cm^2, to achieve a light dose of 0.125 J/cm^2. The stock concentration of BPD in DMSO was determined by spectroscopy immediately prior to each experiment. Upon receipt, calcipotriol was resuspended in DMSO, aliquoted, and stored at −20°C per manufacturer's specifications. DMSO concentration in cell culture media did not exceed 0.1% for all treatments. CAL was thawed immediately prior to each experiment and diluted in culture medium to the appropriate concentration. For conditioned medium (CM) assays, fibroblasts were cultured in serum free DMEM. Treatments were performed 24 hours postplating, and serum-free medium was refreshed 96 hours postplating. Supernatant was collected 144 hours postplating, filtered through a 0.2-μm cellulose filter, and applied to MIA-PaCa-2 or AsPC-1 cells that were plated 24 hours prior. PDAC cells were approximately 80% confluent at this time point. MTT and cell counts were performed on the PDAC cells 96 hours postplating, and normalized metabolic activity was calculated by dividing the corrected NADPH oxidase activity signal (MTT, adjusted to background control) by the average number of cells per well for the group and normalized to the fresh medium control.

Histopathology, αSMA IHC, and masson trichrome staining

Untreated MIA-PaCa-2 and MIA-PaCa-2+PCAF tumors were excised 90 days after implantation and embedded in optimal cutting temperature compound and frozen at −80°C. H&E, IHC staining of αSMA, and Masson trichrome were performed on 20 μm-thick cryosections by the MGH Wellman Center Photopathology Core. A pancreatic pathologist reviewed H&E, Masson trichrome, and αSMA stains of MIA-PaCa-2 alone ($n = 3$ tumors) and MIA-PaCa-2+PCAF ($n = 3$ tumors) tumors and semiquantitatively evaluated the extent (grade 0–3) of desmoplastic fibrosis in each tumor. The pathologic grading criteria to evaluate desmoplasia were as follows: Grade 0 indicated no established desmoplasia; grade 1 indicated few foci with desmoplastic stroma, 10% or fewer of viable tumor nests are associated with desmoplastic stroma; grade 2 indicated that 10%–50% of viable tumor nests were associated with or surrounded by desmoplastic stroma; and grade 3 indicated that >50% of viable tumor nests are associated with/surrounded by desmoplastic stroma. For IHC, briefly, permeabilization was performed with 0.1% Triton X-100 TBS for 15 minutes, tissue sections were blocked with BLOXALL (Vector Laboratories, catalog no. SP-6000) for 15 minutes to block Endogenous Alkaline Phosphatase (AP) and blocked with Protein Block buffer (DAKA, catalog no. X090930-2). Tissue sections were then incubated with anti-alpha Smooth Muscle Actin (Abcam, catalog no. ab5694) antibody overnight at 4°C and incubated with MACH 2 Rabbit AP-Polymer Detection antibody (BioCare Medical, catalog no. RALP525-G) for 30 minutes. Vulcan Fast Red was used for color detection of the antigen-antibody reaction and hematoxylin was used as nuclei counterstain. A whole slide imaging system (Hamamatsu NanoZoomer 2.0-RS) was used to image IHC and Masson Trichrome–stained slides. Analysis of αSMA (shown in red) from the IHC slides, and collagen (shown in blue) from the trichrome slides was performed as described previously (8). Three tumors were excised per condition, and slices were taken evenly across the tumor section. At least six images were taken per condition. Representative images of Masson trichrome and IHC were evenly color balanced using the Nanozoomer viewer software prior to exporting. Only unmodified images were used for quantitative analyses.

Statistical analyses

All results are reported as mean ± SEM unless otherwise specified. Statistical tests were carried out using GraphPad Prism Version 8 (GraphPad Software), in consultation with the MGH Biostatistics Core. Specific tests are indicated in the figure captions. All reported P values are two-tailed unless otherwise specified. *In vivo* results, including fluorescence intensity analyses, (**Figs. 1C–E**, **2C–J,** and **3C–E**; Supplementary Figs. S1C and S1F, S2A–S2C, S3B and S3C, S4B–S4D, S6, and S7B–S7D) were performed using nonparametric tests (Mann–Whitney U test or Kruskal–Wallis one-way ANOVA with appropriate *post hoc* test, Dunn test was used for multiple comparisons); the D'Agostino and Pearson omnibus ($\alpha = 0.05$) and Shapiro–Wilk ($\alpha = 0.05$) normality tests identified deviations from normality. All statements of significance in the results were based on a threshold of $P < 0.05$. No exclusion criteria were used, and no data points or animals were excluded from analysis. Investigators were blinded to experimental groups during tumor volume monitoring.

Data and materials availability

We thank Merrimack Pharmaceuticals for providing nanoliposomal irinotecan (nal-IRI).

Results

PDP + VDR activation enables durable low-dose nal-IRI *in vivo*

We have previously reported that PDP and nal-IRI synergistically interact to control PDAC tumor burden (10). We hypothesized that a triple therapy comprising VDR activation, PDP, and nal-IRI could achieve efficient long-term tumor control at lower nal-IRI doses. To better recapitulate the pancreatic ductal adenocarcinoma (PDAC) microenvironment *in vivo*, an orthotopic xenograft model of PDAC consisting of patient-derived pancreatic CAFs (PCAF; ref. 24) and MIA-PaCa-2 cells was established (Supplementary Fig. S1). PCAFs express functional VDR that translocates to the nucleus following incubation with CAL *in vitro*, indicating VDR activation (Supplementary Fig. S2; ref. 26). Mice bearing PCAF-PDAC xenografts exhibited more established desmoplasia as determined by a pancreatic pathologist's evaluation (grade 2–3 vs. grade 0–1), and significantly greater collagen (Masson Trichrome) and αSMA area compared with a PDAC-only model (Supplementary Fig. S1), suggesting that the *in vivo* coimplantation model may better recapitulate desmoplasia observed in clinical PDAC (4). Mice bearing MIA-PaCa-2+PCAF xenografts, or MIA-PaCa-2 alone, were treated with CAL, PDP, and/or nal-IRI (**Fig. 1A**). Coimplantation mice treated with CAL+PDP+20 mg/kg nal-IRI exhibited prolonged tumor control for 90 days following implantation compared with untreated controls (**Fig. 1B**; Supplementary Fig. S3B. All controls not shown in **Fig. 1B** are shown in Supplementary Fig. S3A). Remarkably, dose deescalation of nal-IRI from 20 to 5 mg/kg did not compromise the efficacy of triple therapy in coimplantation mice (**Fig. 1B** and **C**). While mice treated with the double therapy PDP+20 mg/kg nal-IRI also exhibited prolonged tumor control (**Fig. 1C**), their average tumor mass following excision were not significantly different from untreated mice (Supplementary Fig. S3B). Because mice treated with CAL+20 mg/kg nal-IRI did not exhibit a reduction in tumor volume compared with

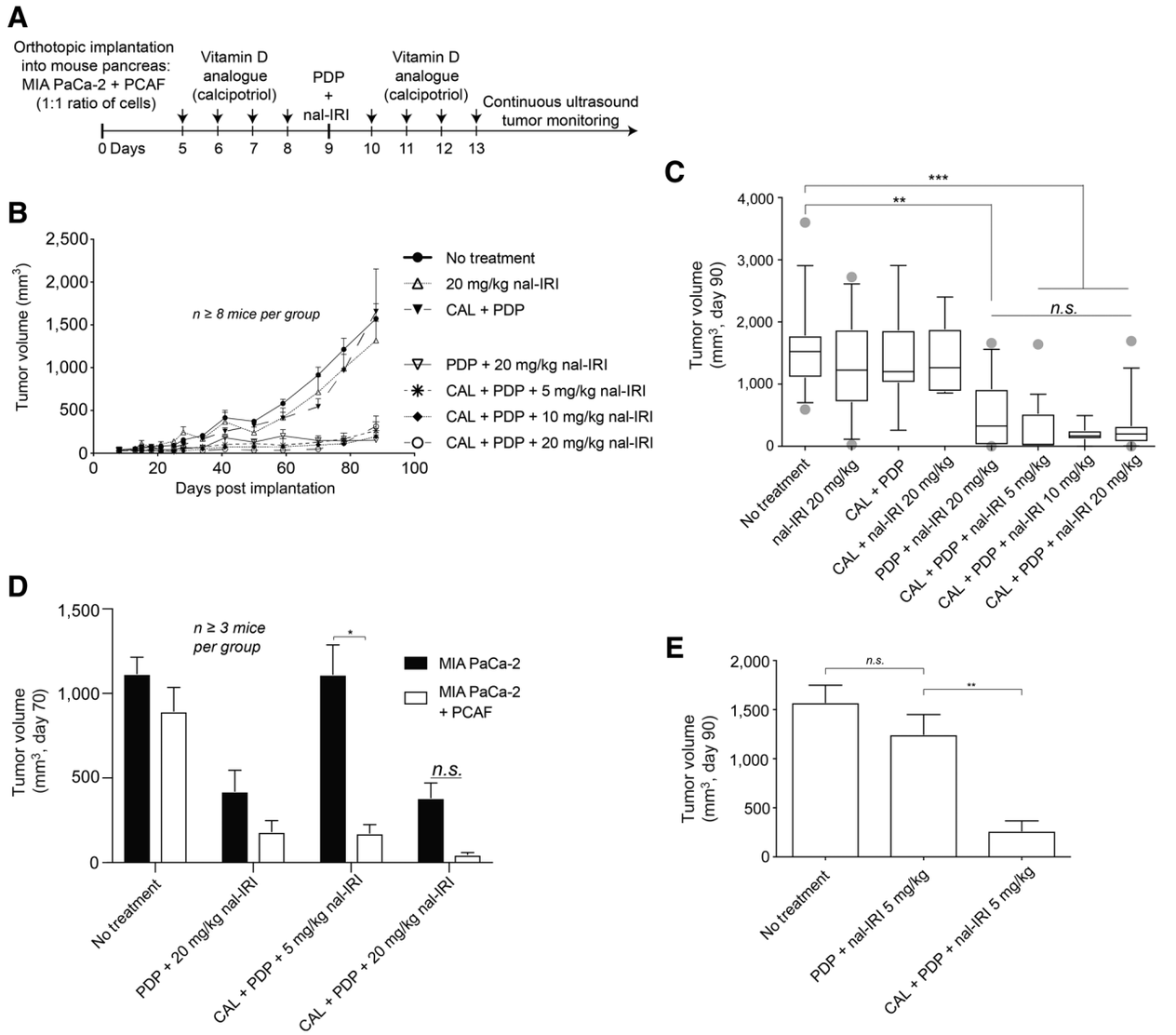

Figure 1.

CAL+PDP enable a 75% dose deescalation of nal-IRI without compromising efficacy. **A,** MIA-PaCa-2 or MIA-PaCa-2 + PCAF were implanted orthotopically into the pancreas of nude mice. CAL treatments were performed daily on days 5–8 and 10–14 postimplantation. PDP and/or nal-IRI were administered on day 9. **B,** MIA-PaCa-2 + PCAF tumors were longitudinally monitored via noninvasive ultrasound imaging. **C,** Tumor volumes were measured near day 90 prior to humane euthanization. Box and whisker plots denoting the 10th–90th percentiles are shown. Mice treated with CAL+PDP+20 mg/kg nal-IRI exhibited prolonged tumor control for up to 90 days following implantation compared with no treatment controls (314.7 ± 120.0 mm^3 vs. $1{,}573 \pm 175.8$ mm^3, $n \geq 14$ mice per condition, $P < 0.001$, Kruskal–Wallis test with Dunn multiple comparison test). There was no difference in the tumor volume of mice treated with CAL+PDP+20 mg/kg nal-IRI versus CAL+PDP+5 mg/kg nal-IRI 90 days postimplantation (314.7 ± 120.0 vs. 265.3 ± 101.0 mm^3, $n \geq 14$ mice per condition, Kruskal–Wallis test with Dunn multiple comparison test). **D,** Seventy days following implantation, MIA-PaCa-2 only tumors treated with CAL+PDP+5 mg/kg nal-IRI were significantly larger than MIA-PaCa-2 + PCAF tumors treated with the same regimen ($1{,}113 \pm 174.5$ mm^3 vs. 174.5 ± 50.2 mm^3; $n \geq 3$ mice per condition, two-tailed t test, $P < 0.05$). **E,** CAL is necessary for durable low-dose triple therapy in mice harboring MIA-PaCa-2 + PCAF xenografts.

untreated controls, the addition of PDP is necessary to yield therapeutic efficacy (**Fig. 1C**). Treatment efficacy was lost following dose deescalation from 20 to 5 mg/kg nal-IRI in MIA-PaCa-2 alone mice treated with triple therapy, suggesting that CAL+PDP sustains treatment efficacy by modulation of the stromal compartment rather than the PDAC cells themselves (**Fig. 1D**). Low-dose double therapy, PDP+5 mg/kg nal-IRI, was ineffective by itself, while the addition of CAL to this regimen resulted in durable tumor control (**Fig. 1E**). Taken together, these data suggest that combined PDP and VDR activation increases the susceptibility of stroma-rich tumors to nal-IRI, and that these therapies act via the tumor stroma to enable a 75% dose deescalation of nal-IRI without compromising long-term tumor control.

Dose deescalation of nal-IRI in the triple therapy regimen significantly decreases morbidity and toxicity

Given the similar treatment response between the triple therapy at 5 and 20 mg/kg nal-IRI, we examined whether this reduction in

chemotherapy dose improved treatment tolerability. Animal body mass was monitored from days 8 to 34 post tumor implantation (**Fig. 2**). Triple therapy with 20 mg/kg nal-IRI caused an 18% reduction in mouse body mass by day 18 compared with untreated animals (**Fig. 2A** and **C**). Approximately 60% of high-dose triple therapy animals exhibited treatment limiting toxicity by day 21, compared with only 16% of triple therapy animals treated with 10 mg/kg nal-IRI and 0% of animals with 5 mg/kg (**Fig. 2B**). Treatment-limiting toxicity was defined as a reduction in body mass of >10%, which meets clinical criteria for cachexia and would be grounds to discontinue treatment (27). Dose deescalation of nal-IRI from 20 to 10 and 5 mg/kg in triple therapy animals resolved this loss of body mass (**Fig. 2C**). By day 34, all animals exhibited body mass that was not significantly different from untreated animals (**Fig. 2D**).

To more sensitively evaluate the toxicity profile of these treatments, the hematologic laboratories alanine aminotransferase (ALT), albumin, hemoglobin (Hb), granulocyte, lymphocyte, and platelet levels were evaluated in untreated animals and those treated with PDP+20 mg/kg nal-IRI, CAL+PDP+5 mg/kg nal-IRI, and CAL+PDP+20 mg/kg nal-IRI. These biomarkers were selected on the basis of the clinical toxicity profile of nal-IRI (28). High-dose triple therapy resulted in a significant elevation in ALT 48 hours after treatment, which resolved following dose deescalation of nal-IRI to 5 mg/kg (**Fig. 2E**). Furthermore, animals in the PDP+20 mg/kg nal-IRI group also experienced elevations in ALT, although not significantly different from untreated animals (**Fig. 2E**). There were no changes in the albumin levels in any of the groups following treatment, suggesting that hepatic synthetic function remained intact in all groups despite the transaminitis (**Fig. 2F**). Triple therapy at 20 mg/kg nal-IRI resulted in a mild but significant drop in Hb and platelet counts, but dose deescalation to 5 mg/kg resolved this issue (**Fig. 2G** and **J**). Although no significant changes were detected in either the granulocyte or lymphocyte counts of in any of the groups (**Fig. 2H** and **I**), these data are confounded by the immunocompromised athymic swiss NU/NU nude mice used in the study.

Dual-targeted stromal modulation suppresses the CXCL12/CXCR7 signaling axis *in vivo*

Although we found that CAL+20 mg/kg nal-IRI does not inhibit tumor growth, activation of VDR is hypothesized to modulate intratumoral paracrine interactions by reprogramming the tumor-associated stroma from an activated to quiescent state at the epigenetic and transcriptomic levels (17, 18). One of the many signaling interactions in the tumor microenvironment is the CXCL12/CXCR7/CXCR4 signaling axis, which has been implicated in the disease progression of several cancers, including PDAC (22, 29).

The impact of PDP and VDR activation on modulation of this axis was evaluated in MIA-PaCa-2 alone and MIA-PaCa-2+PCAF xenografts (**Fig. 3**). Consistent with previous reports (16, 30), PCAFs secreted significantly more CXCL12 *in vitro* compared with MIA-PaCa-2 cells (**Fig. 3A**). CXCR4 and CXCR7 receptors have been shown to be present on MIA-PaCa-2 cells and are responsive to CXCL12 (29).

Expression levels of CXCL12, CXCR4, and CXCR7 in orthotopic tumors were assessed by immunofluorescence *ex vivo* at the end of the treatment period (day 14, **Fig. 3**). Significantly more CXCL12 and CXCR7 were detected in untreated animals bearing MIA-PaCa-2+PCAF xenografts compared with MIA-PaCa-2 alone, suggesting that the presence of CAFs increases intratumoral CXCL12/CXCR7 (**Fig. 3B–D**). Neither CAL nor PDP individually decreased intratumoral CXCL12 nor CXCR7 in coimplantation mice, whereas their combination led to significantly lower expression of both compared with untreated coimplantation animals (**Fig. 3C** and **D**). No appreciable differences in CXCR4 expression were observed in any of the treatment groups at day 14 (**Fig. 3E**). By day 90, statistically significant differences in CXCL12 and CXCR4 expression were detected between untreated MIA-PaCa-2+PCAF and MIA-PaCA-2 alone tumors (Supplementary Fig. S4), suggesting that the PCAFs chronically stimulate this protumorigenic pathway. Furthermore, all treatment groups in MIA-PaCa-2+PCAF animals exhibited statistically similar CXCL12 compared with the untreated animals at this time, suggesting that multi-cycle treatment may be necessary to sustain CXCL12/CXCR7 inhibition.

PDP+CAL interferes with CAF-PDAC paracrine interactions

A CM assay was designed to evaluate the effect of CAL and PDP treatment on paracrine interactions between MIA-PaCa-2 and PCAF cells (**Fig. 4A**). Secretion of CXCL12 following treatment with benzoporphyrin-derivative (BPD) based-PDP at 0.03 μmol/L*J/cm^2 and CAL at 1 μmol/L by PDAC, CAF, and normal fibroblasts (MRC5) was quantified by ELISA. Consistent with previous reports of CAF paracrine secretion, untreated PCAFs and squamous cell carcinoma–associated fibroblasts (SCCAF) exhibited a baseline CXCL12 secretion that was approximately 5-fold higher than MRC5 and MIA-PaCa-2 cells (**Fig. 4B**; refs. 16, 30). Notably, PDP was subcytotoxic for all three fibroblast lines at this dose, whereas CAL induced mild cytotoxicity in MRC5 and SCCAF (Supplementary Fig. S5). Importantly, CAL+PDP was subcytotoxic in the PCAFs (Supplementary Fig. S5). Following CAL+PDP, CXCL12 secretion was reduced by approximately 65% in SCCAFs and 49% in PCAFs compared with untreated controls, correlating with the similar acute reduction observed *in vivo,* while MRC5 and both PDAC lines were unaffected (**Fig. 4B**). Treatment with CAL or PDP individually did not significantly reduce CXCL12 secretion in any of the lines examined here.

To evaluate the impact of CAF-secreted paracrine factors on the metabolic phenotype of PDAC cells, CM from PCAFs and SCCAFs was applied to MIA-PaCa-2 or AsPC-1 cells and metabolic activity per cell was measured. Downstream activity of CXCR4 and CXCR7 has been reported to increase the metabolic activity of PDAC cells (29). CM from both PCAF and SCCAF cells increased the metabolic activity of MIA-PaCa-2 and AsPC-1 cells by 2-fold (**Fig. 4C** and **D**). Although treatment of PCAFs with CAL+PDP abrogated this effect in both PDAC lines, treatment of SCCAFs with this combination was only effective in AsPC-1 cells (**Fig. 4C** and **D**), suggesting that the modulation and effects of secreted paracrine factors is dependent on the CAF origin, consistent with previous reports (31). Notably, the metabolic activity of PDAC cells was unchanged from baseline following exposure to media from MRC5 cells, indicating that any factors secreted by these normal fibroblasts do not grossly affect tumor cell metabolism (Supplementary Fig. S6). To probe whether the observed increase in PDAC metabolic activity was due to the presence of secreted CXCL12 in the CM, 1 ng/mL recombinant CXCL12 (rCXCL12) was applied to PDAC cells in serum-free fresh medium (**Fig. 4C** and **D**). Consistent with previous reports, metabolic activity of both PDAC cell lines increased by approximately 1.5-fold (**Fig. 4C** and **D**; refs. 32, 33). However, this effect was significantly less pronounced than CM from CAFs, suggesting that other secreted factors also contribute to altered cancer cell metabolism (**Fig. 4C** and **D**). To evaluate the specificity of this CXCL12 mediated increase in

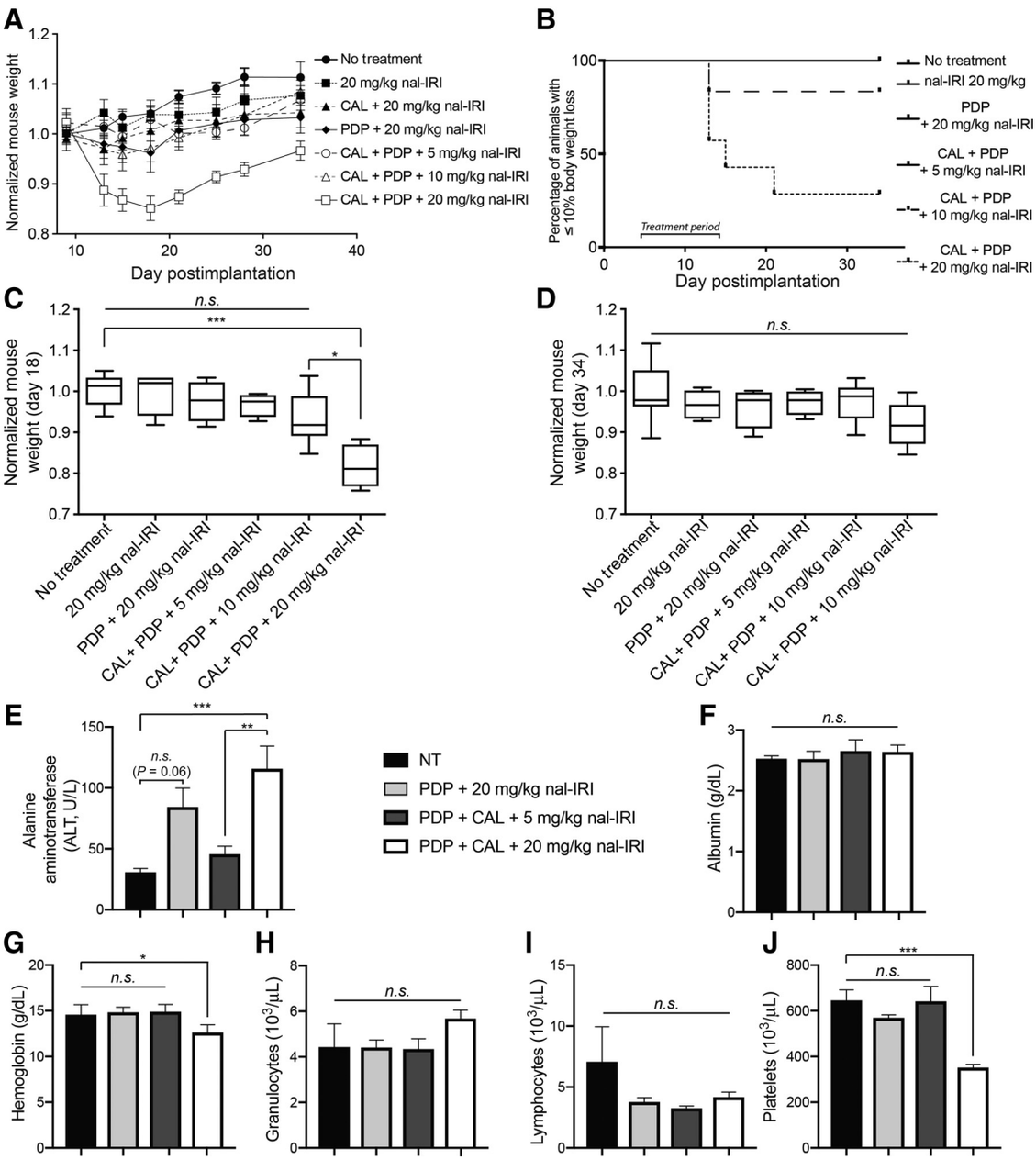

Figure 2.

Dose deescalation of nal-IRI from 20 mg/kg to 5 mg/kg results in decreased toxicity and improved tolerability of triple therapy. **A,** Animal weights were longitudinally monitored every 2–4 days from day 9 to 34 postimplantation. **B,** The percentage of animals whose weight loss exceed 10% of the initial body mass is plotted ($n \geq 6$ animals per group). For the groups in which animal weight loss did not exceed this threshold, a single representative black line is shown (no treatment, 20 mg/kg nal-IRI, PDP+20 mg/kg nal-IRI, and CAL+PDP+5 mg/kg nal-IRI). Normalized animal body mass is plotted 18 days (**C**) and 34 days (**D**) postimplantation. Box and whisker plots denoting the range of the data are shown. The normalized weight of animals treated with CAL+PDP+20 mg/kg nal IRI was significantly lower than those treated with CAL+PDP+5 mg/kg nal-IRI and untreated animals (0.8176 ± 0.023 vs. 1.000 ± 0.015 and 0.9679 ± 0.029, respectively; $n \geq 5$ animals per group, $P < 0.05$, Kruskal–Wallis with Dunn multiple comparisons test). **E,** The serum alanine aminotransferase (ALT; **E**), albumin (**F**), hemoglobin (**G**), granulocyte (**H**), lymphocyte (**I**), and platelet (**J**) levels were determined via analysis of mouse blood. The ALT levels of mice treated with CAL+PDP+20 mg/kg nal-IRI was significantly greater than those treated with CAL+PDP+5 mg/kg nal-IRI and untreated animals (115.5 ± 18.9 U/l vs. 45.4 ± 6.7 U/l and 30.6 ± 3.3 U/l, respectively; $n \geq 5$ animals per group, $P < 0.01$, Kruskal–Wallis with Dunn multiple comparisons test). The ALT of animals treated with CAL+PDP+5 mg/kg nal-IRI was not significantly different from untreated animals (45.4 ± 6.7 U/l vs. 30.6 ± 3.3 U/l; $n \geq 5$ animals per group, Kruskal–Wallis with Dunn multiple comparisons test). Animals in the PDP+20 mg/kg nal-IRI group experienced elevations in ALT, although not significantly different from untreated animals (84.20 ± 15.6 vs. 30.6 ± 3.3; $n \geq 5$ animals per group, $P = 0.06$). The hemoglobin and platelet counts of animals treated with CAL+PDP+20 mg/kg nal-IRI were significantly lower than those treated with CAL+PDP+5 mg/kg nal-IRI and untreated animals ($n \geq 4$ animals per group, $P < 0.05$, Kruskal–Wallis with Dunn multiple comparisons test for each platelet count and hemoglobin count).

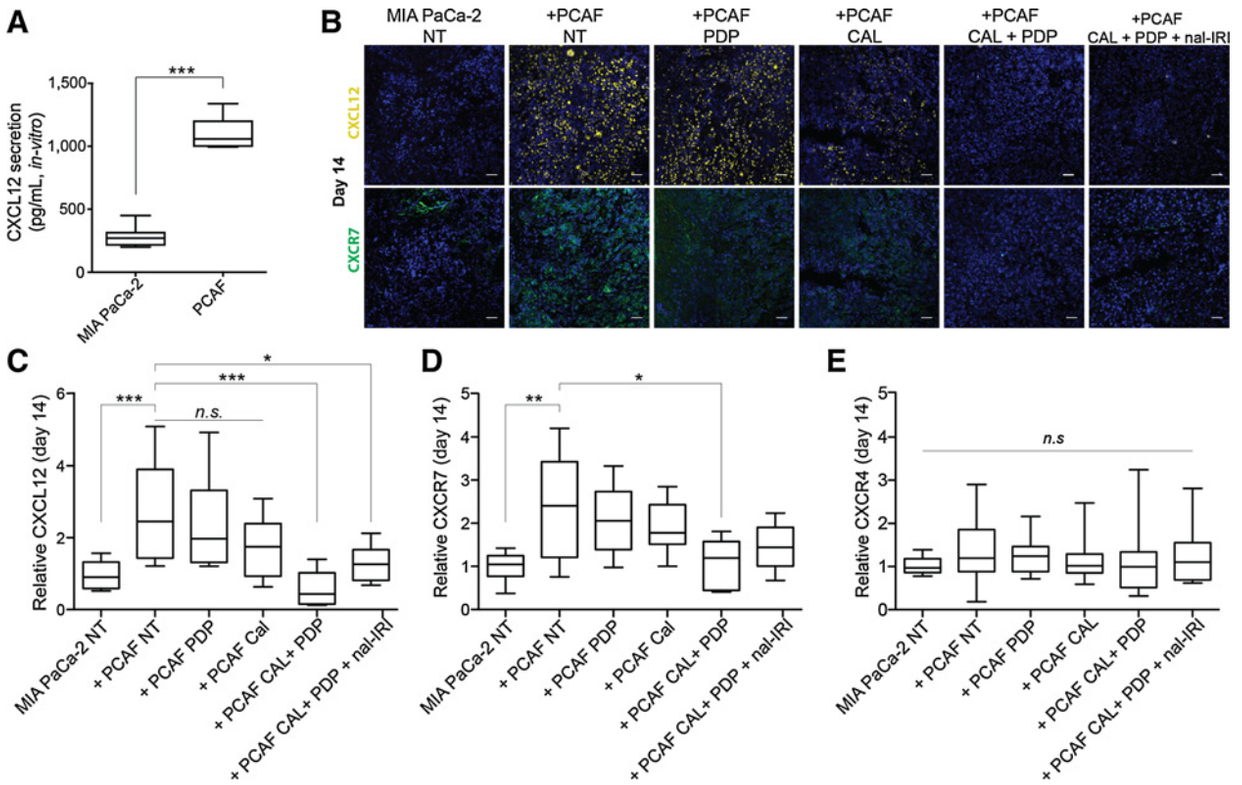

Figure 3.

Cal + PDP reduces CXCL12 and CXCR7 expression *in vivo*. **A,** PCAFs secrete significantly more CXCL12 than MIA-PaCa-2 cells *in vitro* (1,103 ± 47.1 pg/mL vs. 275.5 ± 33.7 pg/mL; $n = 7$ wells per group, $P < 0.001$). **B,** Representative immunofluorescence images are shown of CXCL12 (yellow, top row), CXCR7 (green, bottom row), and DAPI in MIA-PaCa-2 no treatment, and MIA-PaCa-2 + PCAF tumors subjected to (i) no treatment, (ii) PDP, (iii) CAL, (iv) CAL+PDP, (v) CAL+PDP+20 mg/kg nal-IRI 14 days after implantation (corresponding to the end of the treatment period). Scale bars, 50 μm. To quantify immunofluorescence intensities, 6–10 images evenly across the tumor cross section were recorded from at least two tumor samples per condition. The total CXCL12, CXCR7, and CXCR4 fluorescence for each image was normalized to the DAPI area from the same image. **C,** Relative CXCL12 intensity was found to be significantly higher in the +PCAF NT condition compared with MIA-PaCa-2 NT 14 days after implantation (2.81 ± 0.29 vs. 1.01 ± 0.11; $n \geq 20$ images from ≥ 2 animals per group and ≥ 6 slides per animal, $P < 0.001$, Kruskal–Wallis with Dunn multiple comparisons test). Relative CXCL12 intensity for +PCAF CAL+PDP and +PCAF CAL+PDP+nal-IRI was significantly lower than +PCAF NT at the same time point (0.551 ± 0.12 and 1.254 ± 0.15, respectively, vs. 2.805 ± 0.29, $n \geq 12$ images, $P < 0.05$, Kruskal–Wallis with Dunn multiple comparisons test). **D,** Relative CXCR7 intensity was found to be significantly higher in the +PCAF NT condition compared with MIA-PaCa-2 NT 14 days after implantation (2.39 ± 0.32 vs. 1.01 ± 0.09, $n \geq 14$ images, $P < 0.001$, one-way ANOVA with Tukey multiple comparison test). **D,** Relative CXCR7 intensity for +PCAF CAL+PDP was significantly lower than +PCAF NT at the same time point (1.06 ± 0.15 vs. 2.39 ± 0.32, $n \geq 14$ images, $P < 0.05$, One-way ANOVA with Tukey multiple comparison test). **E,** No statistical differences were detected in the CXCR4 intensity at this time point ($n \geq 14$ images, $P = 0.77$, Kruskal–Wallis). Box and whisker plots denoting the 10th–90th percentile of all data are shown in **C–E**.

PDAC metabolic activity and verify its dependency on the canonical CXCL12 signaling axis, PDAC cells were exposed to PCAFs or SCCAF CM, AMD3100, and anti-CXCR7 (**Fig. 4C** and **D**), well-established inhibitors of CXCR4 and CXCR7, respectively (34). PCAF CM + inhibitors caused a significant reduction in the metabolic activity of both PDAC lines compared with PCAF CM alone (**Fig. 4C**), whereas SCCAF CM + inhibitors caused a significant reduction in only AsPC-1 metabolic activity (**Fig. 4D**). These results further support the conclusion that the effects of CXCL12 on PDAC metabolic activity are dependent on the CAF origin. In addition, because there was not a significant difference between the CM + inhibitors and CM+CAL+PDP groups in either PDAC line, it is possible that upstream suppression of CXCL12 induced by CAL+PDP may at least partially phenocopy downstream inhibition of CXCR4 and CXCR7. However, changes in other paracrine interactions also likely occur.

Discussion

Our study suggests that mechanistically diverse approaches, with nonoverlapping toxicities, may be an effective strategy to increase chemotherapy potency. Particularly for PDAC, existing chemotherapeutic regimens require high doses to only modestly extend survival, yet do so at the expense of significant and often life-threatening treatment-induced side effects (2, 35, 36). First-line therapy for locally advanced or metastatic PDAC entails either a combination of 5-fluorouracil (5-FU), leucovorin, oxaliplatin, and irinotecan (FOLFIRINOX), or the less toxic combination of gemcitabine plus abraxane, depending on the patient's performance status (36). nal-IRI, a second-line agent used in combination with 5-FU and leucovorin in the metastatic and gemcitabine-refractory settings, yields a median overall survival of 6 months despite toxicities such as neutropenia, fatigue, diarrhea, vomiting, nausea, asthenia, and abdominal pain (28). Up to 50% of patients treated with nal-IRI and 5-FU may experience

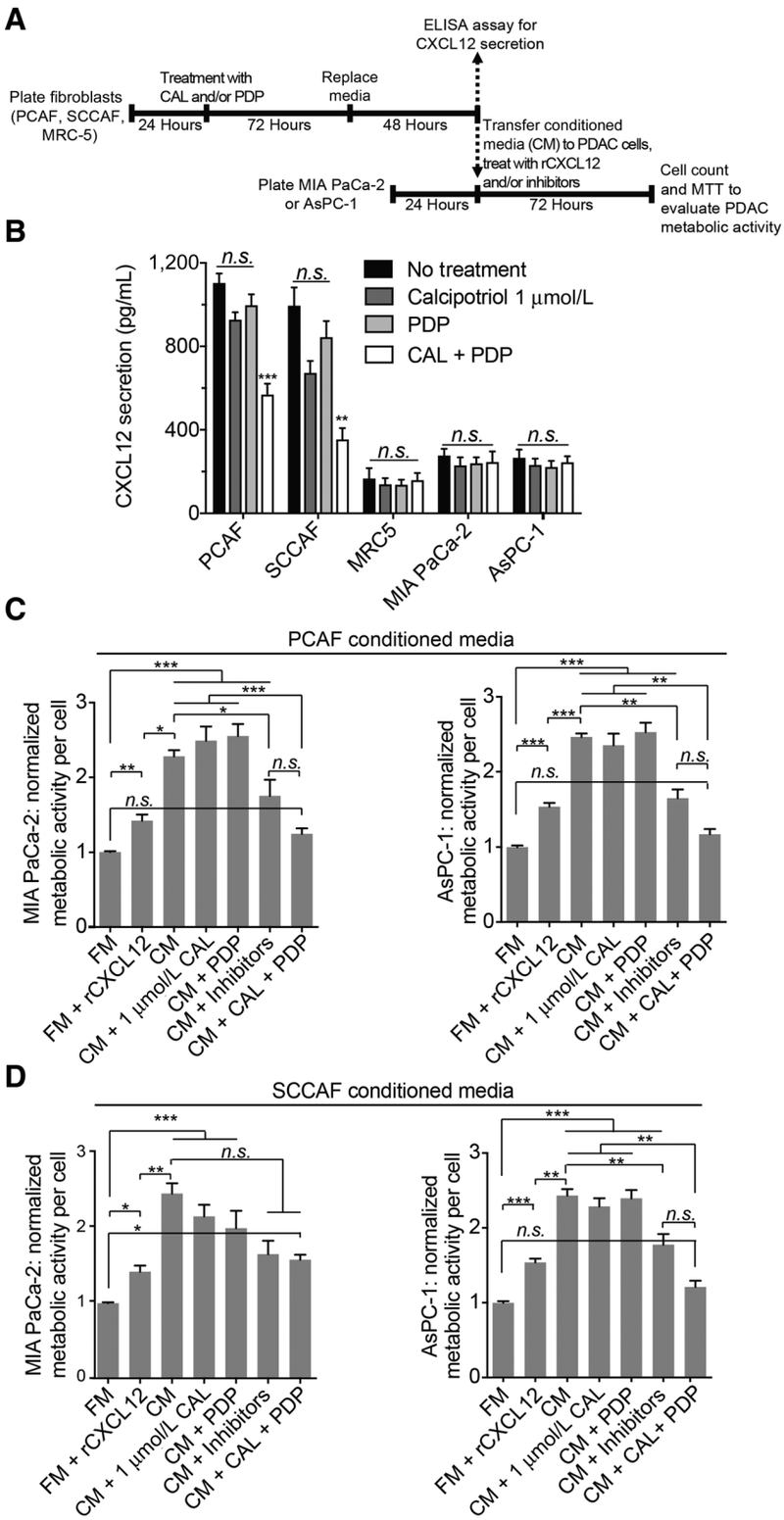

Figure 4.

Cal + PDP abrogates CAF induced changes in metabolic activity in PDAC cells, partially through the CXCL12/CXCR4/CXCR7 signaling axis. **A,** A CM assay was designed to evaluate the impact of secreted paracrine factors from CAFs on PDAC cell metabolic activity. **B,** PDP+CAL was found to significantly reduce the amount of CXCL12 secreted by CAFs, but not normal fibroblasts or PDAC cells ($n = 7$ wells per condition, $P < 0.001$, one-way ANOVA with Tukey test, "PCAF Cal + PDP" vs. "PCAF NT," "SCCAF Cal + PDP" vs. "SCCAF NT"). The impact of recombinant CXCL12 (rCXCL12), PCAF CM (**C**) and SCCAF CM (**D**) on the metabolic activity of MIA PaCa-2 (left) and AsPC-1 (right) cells is plotted. CM from both PCAF and SCCAF cells increased the normalized metabolic activity of MIA-PaCa-2 and AsPC1 cells by over 2-fold (PCAF-MIA-PaCA-2: 2.56 ± 0.16 vs. 1.00 ± 0.014, PCAF-AsPC-1: 2.46 ± 0.049 vs. 1.00 ± 0.020, SCCAF-MIA-PaCa-2: 2.47 ± 0.138 vs. 1.00 ± 0.014, SCCAF-AsPC-1: 2.43 ± 0.086 vs. 1.00 ± 0.02; $n \geq 12$ wells per condition, $P < 0.001$, Kruskal–Wallis with Dunn multiple comparison test). rCXCL12 and CAF CM induced approximately 1.5-fold increase in PDAC cell metabolic activity, although CAF CM induced a significantly greater increase in PDAC cell metabolic activity than rCXCL12 ($n \geq 12$ wells per condition; $P < 0.01$, Kruskal–Wallis with Dunn multiple comparisons test). Treatment of CAFs with CAL+PDP abrogated the CM-induced metabolic activity in PDAC cells ($n \geq 12$ wells per condition, $P < 0.001$, Kruskal–Wallis with Dunn multiple comparisons test, "CM + Cal + PDP" vs. "CM" for all plots) with the exception of MIA-PaCa-2 cells treated with SCCAF CM ($n \geq 12$ wells per condition, difference in rank sum = 57.00, Kruskal–Wallis with Dunn multiple comparisons test, "CM + Cal + PDP" vs. "CM").

severe toxicities, and up to one-third of patients subsequently undergo dose deescalation to attenuate them, likely at the expense of therapeutic efficacy (28). Strategies that enable reduction of the chemotherapy dose without compromising efficacy hold significant promise to increase the clinical utility of these regimens. The data presented here suggest that this may be accomplished via multimodal targeting of

the tumor microenvironment utilizing agents with distinct mechanisms of action.

Photodynamic and biochemical modulation of the tumor microenvironment maintains the efficacy of nal-IRI despite a 75% dose reduction. Production of RMS following photodynamic activation of Visudyne (PDP) permeabilizes the tumor-associated microvasculature (Supplementary methods—tumor vasculature and Dil5-nal-IRI fluorescence imaging; Supplementary Fig. S7) and parenchyma to increase intratumoral nal-IRI (10), while PDP+VDR activation transiently suppress protumorigenic CXCL12/CXCR7/CXCR4 signaling. This combined microenvironmental modulation likely increases the susceptibility of primary PDAC tumors to chemotherapy, enabling substantial dose deescalation while retaining subacute (90-day) disease control (**Fig. 5**).

Although CAL+PDP+nal-IRI, henceforth referred to as triple therapy, with high-dose nal-IRI (20 mg/kg) induces cachexia, ALT transaminitis, decreased hemoglobin and platelet counts, it also affords durable tumor control for up to 90 days postimplantation. The toxicities associated with high dose triple therapy, which are consistent with those seen clinically, were eliminated following a 75% reduction in the administered nal-IRI dose to 5 mg/kg, while 90-day tumor control was maintained. These results were noninferior to those seen with PDP+20 mg/kg nal-IRI, which also demonstrated durable 90-day tumor control. Whether PDP+CAL+5 mg/kg nal-IRI represents a superior strategy to PDP+20 mg/kg nal-IRI from the standpoint of efficacy was not explored in this study. An extended (>90 days) multicycle study that includes an evaluation of metastasis would be required to delineate differences between these groups, as the modulatory effects of CAL+PDP are transient in nature and would likely require multiple cycles to fully capture their benefit. While still amenable for rapid translation, further preclinical study of CAL (or related Vitamin D analogues) + PDP is required for optimization of cycle and dosing parameters. However, our study serves as a proof-of-concept that the combination of CAL+PDP induces beneficial modulatory effects in the tumor and microenvironment which substantially increases the potency of chemotherapy, and lays the groundwork for such follow-up studies.

The most toxic regimen evaluated in this study was PDP+CAL+20 mg/kg nal-IRI. These toxicities were eliminated following dose deescalation to 5 mg/kg, and by all measures investigated in this study, PDP+CAL+5 mg/kg nal-IRI is as tolerable as PDP+20 mg/kg nal-IRI. In the clinical setting, early-phase trials of nal-IRI showed that patients who received lower doses of nal-IRI experience fewer adverse effects than those who received higher doses (37, 38). Because incidence and severity of these side effects are dose dependent, the dual-priming strategy presented here may increase the therapeutic options available for toxicity-sensitive patients who would otherwise be ineligible for full-dose conventional chemotherapy regimens (28). Compared with the standard clinical dose of 70 mg/m^2, the priming strategy described here enables a human-equivalent dose reduction from approximately 60 mg/m^2 to 15 mg/m^2 (20 mg/kg to 5 mg/kg in the mouse; ref. 39). Because paricalcitol, a normocalcemic Vitamin D analogue, and Visudyne-PDT are both FDA approved and under separate clinical investigations for PDAC

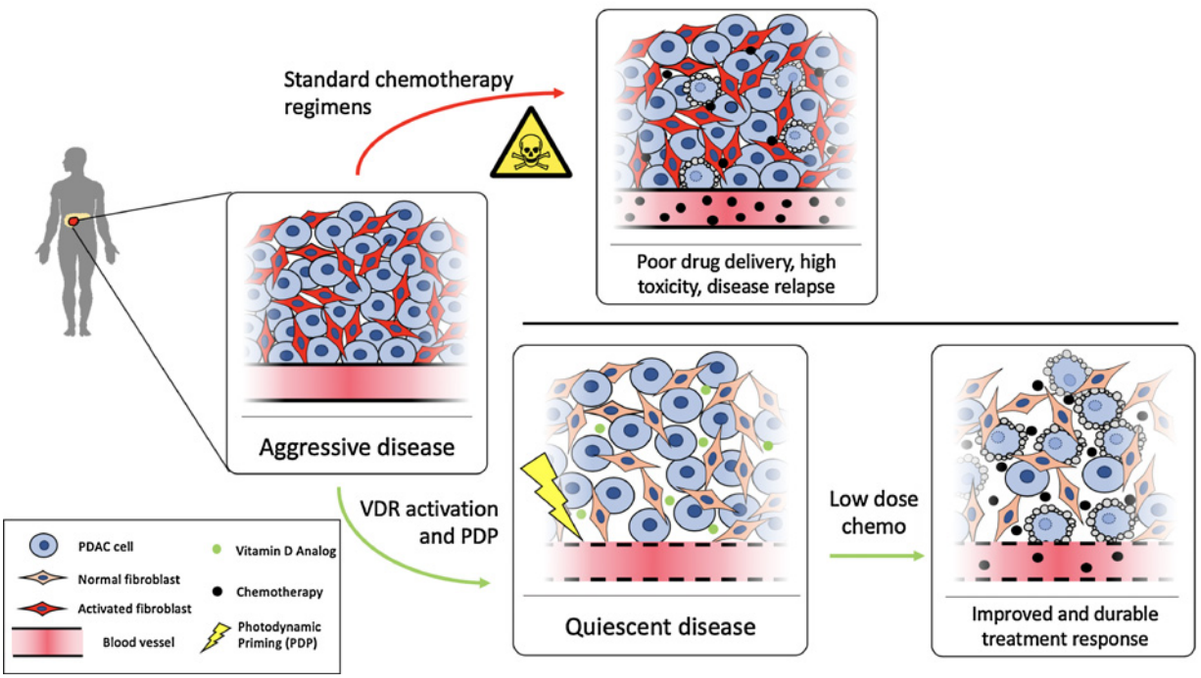

Figure 5.

VDR activation and PDP modulate the tumor microenvironment for effective low-dose chemotherapy. Pancreatic cancer is often detected at a late stage, after activation of fibroblasts and significant desmoplasia. This protumorigenic microenvironment is immunosuppressive, imparts chemo and radioresistance, and promotes disease progression and metastasis. Standard chemotherapy regimens do not address this altered microenvironment, requiring high chemotherapy doses and subsequent toxicity while providing limited nonsustained benefit. Photodynamic and biochemical reprogramming of the tumor stroma results in a disease state that is more susceptible to chemotherapy, allowing lower doses, while maintaining significant and lasting treatment response.

(PDT: NCT03033225; Paracalcitol: NCT03331562, NCT03300921, NCT03520790, NCT03519308), this triple therapy represents a rapidly translatable approach for the management of late-stage PDAC. Further study in the phase I setting would be required to fully characterize the cumulative toxicity that may be associated with PDP + vitamin D, and weigh this against the beneficial modulatory effects of this regimen.

PDP+nal-IRI for PDAC is based on preclinical evidence suggesting that this combination targets nonoverlapping survival pathways to cooperatively and synergistically reduce tumor burden *in vivo* (8). Our findings confirm this synergism in a model that incorporates CAFs, and further demonstrates that VDR activation maintains the efficacy of PDP+nal-IRI despite reducing the chemotherapy dose. Importantly, low-dose triple therapy exhibited minimal efficacy in a PDAC model comprised only of MIA-PaCa-2 cells, suggesting that the improved efficacy observed in the coimplantation model is facilitated by PDP+VDR activation within the stromal compartment. This hypothesis is supported by the fact that PCAF cells exhibit approximately 4-fold more VDR than MIA-PaCa-2 cells (Supplementary Fig. S2B). In addition, VDR activation has been shown to dramatically reduce desmoplasia and increase intratumoral concentrations of chemotherapy in a genetically engineered mouse model of PDAC, a finding not recapitulated in this study perhaps due to limited desmoplasia at the time of treatment (17). Furthermore, the immunocompromised model used in this study may underreport the beneficial immune stimulatory effects that have separately been shown to occur following VDR activation and PDP (12, 16), and further investigation of this CAL+PDP reprogramming strategy is merited in an immunocompetent PDAC model.

Interactions between PDAC cells and the surrounding stromal components have proven to be exceptionally complex. Depletion of the PDAC-associated stroma via hyaluronidase or agents that are cytotoxic to CAFs can induce significant treatment-related toxicities (2) and hyperplasia of primary tumor cells with accelerated disease progression, despite suppression of the surrounding stromal desmoplasia (40). On the basis of a landmark 2009 preclinical study by Olive and colleagues (41), three clinical studies evaluating the safety and efficacy of hedgehog pathway (sHH) inhibition (via the smoothened inhibitors saridigeb and vismodegib) reported that saridigeb + gemcitabine slightly worsened survival in patients with PDA compared with gemcitabine alone (42–44). Similarly, vismodegib + gemcitabine did not improve survival compared to gemcitabine + placebo in two separate trials. Most recently, a clinical trial evaluating the use of pegylated hyaluronidase (PEGPH20) showed that not only does PEGPH20 + mFOLFIRINOX result in a shorter overall survival and progression free survival compared with mFOLFIRINOX alone, PEGPH20 imparted significant adverse events including thromboembolism and gastrointestinal toxicity. The high rate of toxicity associated with this stromal depletion strategy necessitated significant dose delays and reductions, leading to a lower overall mFOLFIRINOX exposure and reduced efficacy (2). A parallel clinical trial that evaluated the efficacy of gemcitabine/nab-paclitacxel with or without PEGPH20 demonstrated that stromal depletion plus chemotherapy acheived prolonged progression-free survival compared with chemotherapy alone only for patients with tumors containing significant amounts of hyaluronic acid. Furthermore, this benefit occurred at the expense of significant thromboembolic events that required anticoagulation prophylaxis (45). These observations support the idea that stromal depletion or ablation could be deleterious. Instead, minimally toxic strategies that modulate the PDAC microenvironment from an activated, or cancer-promoting phenotype, to a quiescent phenotype, without directly killing or depleting stroma, could be more effective in simultaneously reducing toxicity and improving efficacy of anti-PDAC regimens (17, 18).

Because CAL+PDP+5 mg/kg nal-IRI was equivalent to PDP+20 mg/kg nal-IRI in terms of efficacy and toxicity, we evaluated the global transcriptomic profiles of tumors following these two regimens (day 14 postimplantation) to investigate whether there were differences in treatment induced biomolecular changes (supplemental methods–RNA extraction and sequencing). A selected group of significantly altered genes of interest are shown in Supplementary Fig. S8. In general, tumors of mice treated with PDP+20 mg/kg nal-IRI expressed lower levels of tumor suppressor genes, such as miR-145, cyclin-dependent kinase inhibitor (CDKN2A), Gasdermin D (GSDMD), Leucine zipper, downregulated in cancer 1 (LDOC1) and Forkhead Box S1 (FOXS1), while PDP+CAL+5 mg/kg nal-IRI had a minimal effect on expression of these genes. Furthermore, PDP + 20 mg/kg nal-IRI–treated tumors exhibited higher expression of tumor promoters, such as Denticleless E3 Ubiquitin Protein Ligase Homolog (DTL) and E2F Transcription Factor 7 and 8 (E2F7/E2F8), as well as genes involved in DNA repair, including Breast cancer type 1 susceptibility protein 1 and 2 (BRCA1/BRCA2), DNA Polymerase Theta (POLQ), and X-Ray Repair Cross Complementing 2 (XRCC2). Similarly, PDP+CAL+5 mg/kg nal-IRI had a minor suppressive effect on the expression of these genes. Importantly, these transcriptomic profiles represent the surviving cell populations following treatment, as the majority of cell death has likely occurred by this time. As a whole, the addition of CAL and deescalation of nal-IRI appears to alter the global transcriptomic profile of stroma-containing tumors in such a way that may make them less aggressive and more susceptible to further cytotoxic therapy in the acute setting.

Sherman and colleagues (17) demonstrated through *in vitro* studies and animal models that CAL reprogrammed the stromal compartment to a quiescent phenotype, reduced desmoplasia, and potentiated gemcitabine efficacy. Given the immense complexity of VDR activation and its multifactorial effects on downstream cellular pathways, the specific consequences of VDR activation on PDAC-stromal paracrine crosstalk are incompletely understood (18). In our model, CAL by itself or in combination with nal-IRI was insufficient for long-term tumor control. Durable tumor control could only be achieved when CAL+PDP were administered in combination with chemotherapy, which correlated with acute suppression of CXCL12 both *in vivo* and *in vitro*. To our knowledge, this is the first study to provide evidence that VDR activation in combination with PDP suppresses PDAC-stromal CXCL12/CXCR7 signaling, and that this suppression, perhaps secondary to stromal reprogramming, correlates with improved tumor control *in vivo*.

Pancreatic cancer cell lines and resected tumors have been shown to express CXCR4 and CXCR7, and exhibit context dependent interactions with CXCL12 (22, 29). AMD3100, an antagonist of CXCR4, is currently in clinical trials for a variety of cancers due to its ability to suppress this signaling pathway (NCT03277209, NCT03746080). Although promising, suppression of CXCR4 alone is unlikely to completely eliminate the protumorigenic effects of CXCL12 due to compensatory CXCL12/CXCR7 signaling, as well as recent evidence suggesting that AMD3100 may allosterically agonize CXCR7 (46). This study demonstrates that PDP+VDR activation transiently suppresses CXCL12 and CXCR7 *in vivo,* whereas CXCR4 expression remains unaffected. Our *in vitro* data suggest that PDP+VDR activation directly modulates CAF secretion of CXCL12, upstream from the receptor target of AMD3100 and related therapies. Given that recombinant CXCL12 does not increase PDAC metabolic activity to

the same extent as CAF CM, there are likely additional paracrine factors secreted by CAFs that induce an aggressive phenotype in PDAC cells. This hypothesis is supported by the finding that pretreatment of PDAC cells with inhibitors to CXCR4 and 7 (AMD3100 and anti-CXCR7) does not totally abrogate the effect of CAF CM on cancer cells, an observation that has also been described previously (47). However, because PDP+CAL does prevent CAF CM from increasing PDAC cell metabolic activity, we postulate that the modulatory effects of this combination extend beyond the CXCL12/CXCR4/CXCR7 signaling axis. Because the biological consequences of Vitamin D and PDP are extensive, it is likely that the biomolecular mechanisms for improved chemotherapy efficacy observed in this study are due to modulation of multiple converging pathways. While our mechanistic observations are consistent with the treatment response outcomes, it is exciting to envision a more in-depth study at the genomic/transcriptomic level that will elucidate the relationships between these molecular pathways and treatment outcomes.

In summary, we propose that advanced stage tumors, which require complex disease sustaining interactions with stroma to facilitate progression and drug resistance, can be more humanely managed with multi-modal strategies that prime the microenvironment for enhanced tumor responsiveness to chemotherapy. The rapidly translatable strategy presented in this study leverages a mechanistically diverse approach, based on PDP and stromal reprogramming, to offer a new perspective on simultaneously prioritizing treatment and tolerability. This strategy challenges the prevailing paradigm that increasing both the efficacy and tolerability of an anticancer regimen are mutually exclusive endpoints.

Disclosure of Potential Conflicts of Interest

No potential conflicts of interest were disclosed.

Authors' Contributions

Conception and design: S. Anbil, M. Pigula, H.-C. Huang, E.V. Maytin, I. Rizvi, T. Hasan

Development of methodology: S. Anbil, M. Pigula, H.-C. Huang, S. Mallidi, M. Broekgaarden, Y. Baglo, T. Hasan

Acquisition of data (provided animals, provided facilities, etc.): S. Anbil, M. Pigula, H.-C. Huang, S. Mallidi, Y. Baglo, P.D. Silva, M. Mino-Kenudson

Analysis and interpretation of data (e.g., statistical analysis, biostatistics, computational analysis): S. Anbil, M. Pigula, H.-C. Huang, S. Mallidi, M. Broekgaarden, P.D. Silva, M. Mino-Kenudson, I. Rizvi, T. Hasan

Writing, review, and/or revision of the manuscript: S. Anbil, M. Pigula, H.-C. Huang, S. Mallidi, M. Broekgaarden, Y. Baglo, P.D. Silva, D.M. Simeone, M. Mino-Kenudson, E.V. Maytin, I. Rizvi, T. Hasan

Administrative, technical, or material support (i.e., reporting or organizing data, constructing databases): S. Anbil, M. Pigula, T. Hasan

Study supervision: I. Rizvi, T. Hasan

Acknowledgments

This work was conducted with support from the Photopathology Center of the Wellman Center for Photomedicine and the Biostatistics Core of Massachusetts General Hospital. We thank Gian-Paulo Dotto and Sandro Goruppi of the MGH Cutaneous Biology Research Center for their generous gift of squamous cell carcinoma–associated fibroblasts. This work was supported by NIH grants P01CA084203 (to T. Hasan), UH3CA189901 (to T. Hasan), and S10ODO1232601 (to T. Hasan), K99CA194269 (to H.C. Huang), R00CA194269 (to H.C. Huang), and R00CA175292 (to I. Rizvi). S. Anbil was a Howard Hughes Medical Institute Medical Research Fellow.

The costs of publication of this article were defrayed in part by the payment of page charges. This article must therefore be hereby marked *advertisement* in accordance with 18 U.S.C. Section 1734 solely to indicate this fact.

Received August 12, 2019; revised December 8, 2019; accepted March 12, 2020; published first March 27, 2020.

References

1. Tempero M, Malafa M, Al-Hawary M, Asbun H, Behrman SW, Benson AB III, et al. National Comprehensive Cancer Network guidelines: pancreatic adenocarcinoma, version 1; 2019. Available from: https://jnccn.org/view/journals/jnccn/17/3/article-p202.xml.
2. Ramanathan RK, McDonough SL, Philip PA, Hingorani SR, Lacy J, Kortmansky JS, et al. Phase IB/II randomized study of FOLFIRINOX plus pegylated recombinant human hyaluronidase versus FOLFIRINOX alone in patients with metastatic pancreatic adenocarcinoma: SWOG S1313. J Clin Oncol 2019;37:1062–9.
3. Cirri P, Chiarugi P. Cancer-associated-fibroblasts and tumour cells: a diabolic liaison driving cancer progression. Cancer Metastasis Rev 2012;31:195–208.
4. Neesse A, Michl P, Frese KK, Feig C, Cook N, Jacobetz MA, et al. Stromal biology and therapy in pancreatic cancer. Gut 2011;60:861–8.
5. Spadi R, Brusa F, Ponzetti A, Chiappino I, Birocco N, Ciuffreda L, et al. Current therapeutic strategies for advanced pancreatic cancer: a review for clinicians. World J Clin Oncol 2016;7:27–43.
6. Huggett MT, Jermyn M, Gillams A, Illing R, Mosse S, Novelli M, et al. Phase I/II study of verteporfin photodynamic therapy in locally advanced pancreatic cancer. Br J Cancer 2014;110:1698–704.
7. DeWitt JM, Sandrasegaran K, O'Neil B, House MG, Zyromski NJ, Sehdev A, et al. Phase 1 study of EUS-guided photodynamic therapy for locally advanced pancreatic cancer. Gastrointest Endosc 2019;89:390–8.
8. Huang HC, Mallidi S, Liu J, Chiang CT, Mai Z, Goldschmidt R, et al. Photodynamic therapy synergizes with irinotecan to overcome compensatory mechanisms and improve treatment outcomes in pancreatic cancer. Cancer Res 2016;76:1066–77.
9. Yu C-H, Yu C-C. Photodynamic therapy with 5-aminolevulinic acid (ALA) impairs tumor initiating and chemo-resistance property in head and neck cancer-derived cancer stem cells. PLoS One 2014;9:e87129.
10. Huang H-C, Rizvi I, Liu J, Anbil S, Kalra A, Lee H, et al. Photodynamic priming mitigates chemotherapeutic selection pressures and improves drug delivery. Cancer Res 2018;78:558–71.
11. Snyder JW, Greco WR, Bellnier DA, Vaughan L, Henderson BW. Photodynamic therapy: a means to enhanced drug delivery to tumors. Cancer Res 2003;63:8126–31.
12. Mroz P, Hashmi JT, Huang Y-Y, Lange N, Hamblin MR. Stimulation of anti-tumor immunity by photodynamic therapy. Expert Rev Clin Immunol 2011;7:75–91.
13. Spring BQ, Rizvi I, Xu N, Hasan T. The role of photodynamic therapy in overcoming cancer drug resistance. Photochem Photobiol Sci 2015;14:1476–91.
14. Spring BQ, Bryan Sears R, Zheng LZ, Mai Z, Watanabe R, Sherwood ME, et al. A photoactivable multi-inhibitor nanoliposome for tumour control and simultaneous inhibition of treatment escape pathways. Nat Nanotechnol 2016;11:378–87.
15. Erkan M, Hausmann S, Michalski CW, Fingerle AA, Dobritz M, Kleeff J, et al. The role of stroma in pancreatic cancer: diagnostic and therapeutic implications. Nat Rev Gastroenterol Hepatol 2012;9:454–67.
16. Feig C, Jones JO, Kraman M, Wells RJB, Deonarine A, Chan DS, et al. Targeting CXCL12 from FAP-expressing carcinoma-associated fibroblasts synergizes with anti-PD-L1 immunotherapy in pancreatic cancer. Proc Natl Acad Sci U S A 2013;110:20212–7.
17. Sherman MH, Yu RT, Engle DD, Ding N, Atkins AR, Tiriac H, et al. Vitamin D receptor-mediated stromal reprogramming suppresses pancreatitis and enhances pancreatic cancer therapy. Cell 2014;159:80–93.
18. Sherman MH, Yu RT, Tseng TW, Sousa CM, Liu S, Truitt ML, et al. Stromal cues regulate the pancreatic cancer epigenome and metabolome. Proc Natl Acad Sci U S A 2017;114:1129–34.

19. Gollnick SO, Evans SS, Baumann H, Owczarczak B, Maier P, Vaughan L, et al. Role of cytokines in photodynamic therapy-induced local and systemic inflammation. Br J Cancer 2003;88:1772–9.
20. Kammerer R, Buchner A, Palluch P, Pongratz T, Oboukhovskij K, Beyer W, et al. Induction of immune mediators in glioma and prostate cancer cells by non-lethal photodynamic therapy. PLoS One 2011;6:e21834.
21. Domanska UM, Kruizinga RC, Nagengast WB, Timmer-Bosscha H, Huls G, de Vries EGE, et al. A review on CXCR4/CXCL12 axis in oncology: no place to hide. Eur J Cancer 2013;49:219–30.
22. Sun X, Cheng G, Hao M, Zheng J, Zhou X, Zhang J, et al. CXCL12/CXCR4/CXCR7 chemokine axis and cancer progression. Cancer Metastasis Rev 2010;29:709–22.
23. Guo J-C, Li J, Zhou L, Yang J-Y, Zhang Z-G, Liang Z-Y, et al. CXCL12-CXCR7 axis contributes to the invasive phenotype of pancreatic cancer. Oncotarget 2016;7:62006–18.
24. Waghray M, Yalamanchili M, Dziubinski M, Zeinali M, Erkkinen M, Yang H, et al. GM-CSF mediates mesenchymal-epithelial cross-talk in pancreatic cancer. Cancer Discov 2016;6:886–99.
25. Pigula M, Huang H-C, Mallidi S, Anbil S, Liu J, Mai Z, et al. Size-dependent tumor response to photodynamic therapy and irinotecan monotherapies revealed by longitudinal ultrasound monitoring in an orthotopic pancreatic cancer model. Photochem Photobiol 2019;95:378–86.
26. Racz A, Barsony J. Hormone-dependent translocation of vitamin D receptors is linked to transactivation. J Biol Chem 1999;274:19352–60.
27. Davis MP, Dickerson ED. Cachexia and anorexia: cancer's covert killer. Support Care Cancer 2000;8:180–7.
28. Ipsen. Onivyde (package insert); 2017. Available from: https://www.ipsen.com/websites/Ipsen_Online/wp-content/uploads/sites/9/2020/04/10140532/ONV-US-000771-Onivyde-Promotional-PI-8.5-x-11.pdf.
29. Heinrich EL, Lee W, Lu J, Lowy AM, Kim J. Chemokine CXCL12 activates dual CXCR4 and CXCR7-mediated signaling pathways in pancreatic cancer cells. J Transl Med 2012;10:68.
30. Demir IE, Kujundzic K, Pfitzinger PL, Saricaoglu ÖC, Teller S, Kehl T, et al. Early pancreatic cancer lesions suppress pain through CXCL12-mediated chemoattraction of Schwann cells. Proc Natl Acad Sci U S A 2017;114:E85–94.
31. Sazeides C, Le A. Metabolic relationship between cancer-associated fibroblasts and cancer cells. Adv Exp Med Biol 2018;1063:149–65.
32. Shen B, Zheng M-Q, Lu J-W, Jiang Q, Wang T-H, Huang X-E. CXCL12-CXCR4 promotes proliferation and invasion of pancreatic cancer cells. Asian Pacific J Cancer Prev 2013;14:5403–8.
33. Singh S, Srivastava SK, Bhardwaj A, Owen LB, Singh AP. CXCL12–CXCR4 signalling axis confers gemcitabine resistance to pancreatic cancer cells: a novel target for therapy. Br J Cancer 2010;103:1671–9.
34. Hatse S, Princen K, Bridger G, De Clercq E, Schols D. Chemokine receptor inhibition by AMD3100 is strictly confined to CXCR4. FEBS Lett 2002;527:255–62.
35. Conroy T, Desseigne F, Ychou M, Bouché O, Guimbaud R, Bécouarn Y, et al. FOLFIRINOX versus gemcitabine for metastatic pancreatic cancer. N Engl J Med 2011;364:1817–25.
36. Ryan D. Chemotherapy for advanced exocrine pancreatic cancer - UpToDate; 2019. Available from: https://www.uptodate.com/contents/chemotherapy-for-advanced-exocrine-pancreatic-cancer.
37. Chen L, Chang T, Cheng A, Yang C, Shiah H, Chang J, et al. Phase I study of liposome encapsulated irinotecan (PEP02) in advanced solid tumor patients. J Clin Oncol 2008;26:2565.
38. Ko AH, Tempero MA, Shan YS, Su WC, Lin YL, Dito E, et al. A multinational phase 2 study of nanoliposomal irinotecan sucrosofate (PEP02, MM-398) for patients with gemcitabine-refractory metastatic pancreatic cancer. Br J Cancer 2013;109:920–5.
39. USFDA Guidance for Industry: estimating the maximum safe Starting dose in initial clinical trials for therapeutics in adult healthy volunteers; 2005. Available from: https://www.fda.gov/media/72309/download.
40. Özdemir BC, Pentcheva-Hoang T, Carstens JL, Zheng X, Wu C-C, Simpson TR, et al. Depletion of carcinoma-associated fibroblasts and fibrosis induces immunosuppression and accelerates pancreas cancer with reduced survival. Cancer Cell 2014;25:719–34.
41. Olive KP, Jacobetz MA, Davidson CJ, Gopinathan A, McIntyre D, Honess D, et al. Inhibition of Hedgehog signaling enhances delivery of chemotherapy in a mouse model of pancreatic cancer. Science 2009;324:1457–61.
42. Ko AH, LoConte N, Tempero MA, Walker EJ, Kate Kelley R, Lewis S, et al. A phase I study of FOLFIRINOX plus IPI-926, a Hedgehog pathway inhibitor, for advanced pancreatic adenocarcinoma. Pancreas 2016;45:370–5.
43. Kim EJ, Sahai V, Abel EV, Griffith KA, Greenson JK, Takebe N, et al. Pilot clinical trial of Hedgehog pathway inhibitor GDC-0449 (vismodegib) in combination with gemcitabine in patients with metastatic pancreatic adenocarcinoma. Clin Cancer Res 2014;20:5937–45.
44. Catenacci DVT, Junttila MR, Karrison T, Bahary N, Horiba MN, Nattam SR, et al. Randomized phase Ib/II study of gemcitabine plus placebo or vismodegib, a Hedgehog pathway inhibitor, in patients with metastatic pancreatic cancer. J Clin Oncol 2015;33:4284–92.
45. Hingorani SR, Zheng L, Bullock AJ, Seery TE, Harris WP, Sigal DS, et al. HALO 202: randomized phase II study of PEGPH20 plus nab-paclitaxel/gemcitabine versus nab-paclitaxel/gemcitabine in patients with untreated, metastatic pancreatic ductal adenocarcinoma. J Clin Oncol 2018;36:359–66.
46. Kalatskaya I, Berchiche YA, Gravel S, Limberg BJ, Rosenbaum JS, Heveker N. AMD3100 is a CXCR7 ligand with allosteric agonist properties. Mol Pharmacol 2009;75:1240–7.
47. Gao Z, Wang X, Wu K, Zhao Y, Hu G. Pancreatic stellate cells increase the invasion of human pancreatic cancer cells through the stromal cell-derived factor-1/CXCR4 axis. Pancreatology 2010;10:186–93.